Optical properties of PM2.5 particles: Results from a monitoring campaign in southeastern Italy

Salvatore Romano[a,*], Maria Rita Perrone[a], Giulia Pavese[b], Francesco Esposito[c], Mariarosaria Calvello[b]

[a] *Dipartimento di Matematica e Fisica, Università del Salento, Lecce, Italy*
[b] *Istituto di Metodologie per l'Analisi Ambientale, Consiglio Nazionale delle Ricerche, Potenza, Italy*
[c] *Scuola di Ingegneria, Università della Basilicata, Potenza, Italy*

A B S T R A C T

The performance of aerosol classification schemes based on intensive optical parameters and applied to mixed particle populations monitored at the surface has been investigated to test the ability of optical parameters to identify different types of particles/particle mixtures and explore their complex features. The results show that the combination of two intensive optical parameters does not allow for the unique identification of different particle types. The classification scheme based on the Absorption Ångström Exponent (AAE) as a function of the Scattering Ångström Exponent (SAE) and color-coded by the Single Scattering Albedo difference (dSSA) is a good graphical framework to discriminate between different types of particle/particle mixtures. This aerosol classification scheme has been applied to study the optical properties of heterogeneous PM2.5 particles that were monitored at a coastal site of the Central Mediterranean and were significantly affected by both natural and anthropogenic sources also because of long-range transport from surrounding countries. The calculated AAE, SAE, and dSSA hourly means smoothly and continuously vary within their respective range (0.6–3.4, −0.7–3.0, and −0.33–0.52, respectively) because of the different mixing degree of different types of particles. Consequently, the main features of the particle populations depend on the range of the AAE, SAE, and dSSA values. Eight different clusters have been selected within the used graphical framework to identify four key particle populations (dust, marine, OC-dominated, and BC-dominated particles) and four particle mixtures dominated by key aerosol populations. In addition, their main features have been characterized. Particle mixtures consisting of large and low-absorbing particles (LLAP), small and high-absorbing particles (SHAP), dominated by dust, and large organic particles have been characterized. Marine, LLAP, and mixed dust clusters with a SAE value below 1 are responsible for aerosol scattering coefficients (σ_s; at 470 nm) below $100\,\mathrm{Mm}^{-1}$. Conversely, SHAP, BC-dominated, and OC-based mixtures are responsible for the highest σ_s values and represent dominant particles species.

1. Introduction

Natural and anthropogenic atmospheric aerosols play an essential role in the Earth's radiation budget. They significantly influence the climate system on local, regional, and global scales, directly by scattering and absorbing the solar and terrestrial radiation (e.g., Coakley et al., 1983; Haywood and Shine, 1995; Yu et al., 2006) and indirectly by acting as cloud and ice condensation nuclei (e.g., Rosenfeld and Lensky, 1998; Lohmann and Feichter, 2005). As recently stated in Intergovernmental Panel on Climate Change – IPCC's Fifth Assessment Report on Climate Change (2013), the contribution of aerosol particles represents one of the largest uncertainties in the estimates of the total radiative effect. This can be mostly attributed to the high spatial and temporal variability of the aerosol particle concentrations, chemical composition, shape, refractive index, size, vertical distribution, and water uptake (e.g., Kaufman et al., 2002; Masmoudi et al., 2003; Kinne et al., 2006). Because aerosol particles can be transported over long distances up to the intercontinental scale (e.g., Chin et al., 2007; Yu et al., 2013), their optical and microphysical properties may change because of their interactions and mixing, leading to significant variations of their radiative effect. Consequently, long-term and global monitoring of aerosol concentrations and properties and the

---

identification of the main aerosol types are fundamental to better predict their climatic effects.

Aerosol types with significant light-scattering properties mainly include organic particles, water-soluble inorganic species, such as sulphates or nitrates generally associated with fossil fuel/biomass combustion, and ammonium from fertilizers or biological sources (e.g., Charlson et al., 1992; Ten Brink et al., 1996; Haywood and Ramaswamy, 1998; Zhang et al., 2012). Mineral dust and sea salt may also significantly contribute to light scattering (e.g., Li et al., 1996; Lowenthal and Kumar, 2006; Nousiainen and Kandler, 2015). Carbonaceous particles are important light-absorbing species of the aerosol population (e.g., Cazorla et al., 2013; Costabile et al., 2013). On one side, there is black carbon (BC), refractory material that strongly absorbs light over a broad spectral range. Then, there is the colorless organic carbon (OC), non-refractory material, with no absorption or low absorption in the ultraviolet–visible (UV–vis) spectral range (e.g., Costabile et al., 2017). The term brown carbon (BrC) has recently emerged in the scientific literature (e.g., Andreae and Gelencsér, 2006; Bahadur et al., 2012) to describe colored organic compounds with an absorption spectrum smoothly increasing from the visible to the near-UV wavelengths, with a strong wavelength dependence of the light absorption coefficient (λ^{-2} - λ^{-6}) according to Costabile et al. (2017, and references therein). Mineral dust is also a light-absorbing species of the aerosol population (e.g., Yang et al., 2009; Rizzo et al., 2011).

Nephelometers and aethalometers are widely used to monitor aerosol scattering and absorption coefficients, respectively, which represent the main extensive optical parameters characterizing aerosol populations. Based on these extensive parameters, different intensive aerosol optical properties can be calculated such as the Scattering and Absorption Ångström Exponents (SAEs and AAEs), respectively, which represent the wavelength dependence of the scattering and absorption coefficients, and the single scattering albedo (SSA) and its wavelength dependence (dSSA). Intensive optical properties are commonly used to identify different aerosol types, which have to be known to characterize the aerosol's role in atmospheric processes, detect the main aerosol sources, improve aerosol satellite retrieval algorithms, and validate climate models (Russell et al., 2014). Therefore, different combinations of aerosol-scattering and -absorbing intensive parameters were used to define many classification schemes, as summarized by Schmeisser et al. (2017). Most of them are based on the AAE vs. SAE plot to visualize the relationships between aerosol optical properties and identify corresponding aerosol types (e.g., Yang et al., 2009; Russell et al., 2010; Bahadur et al., 2012; Lee et al., 2012). The SAE is mainly related to the aerosol size distribution (Schuster et al., 2006), while the AAE depends on the composition of the absorbing aerosol (Bergstrom et al., 2007; Russell et al., 2010). Therefore, a unique combination of the two selected intensive parameters is associated with a particular aerosol type. Cazorla et al. (2013) and Cappa et al. (2016) designated low SAE values in combination with high AAE values as representative of dust or dust mixed with BC or BrC. In contrast, high SAE values in combination with AAE values of ∼1 are considered representative of aerosol populations dominated by BC. Cazorla et al. (2013) combined AAE and SAE values derived from ten AErosol RObotic NETwork (AERONET) sites in California (USA) to deduce the chemical particle speciation from the spectral dependence of the particle optical properties. They validated the methodology they developed by *in situ* measurements of the particle optical properties and chemical composition during three aircraft field campaigns in 2010 and 2011. A clear predominance of mixed aerosol types was observed during the aircraft field campaigns. The methodology proposed by Cazorla et al. (2013) was then updated by Cappa et al. (2016) to investigate the optical properties of the PM1, PM2.5, and PM10 fractions during the 2010 field campaign of the Carbonaceous Aerosols and Radiative Effects Study (CARES) in California (USA). They demonstrated that optical property measurements can be used to assess chemical differences of contributing particle types, identify key particulate matter (PM) sources, and establish discrepancies in the

behavior of sub- and supermicron PM. The SSA (e.g., Yang et al., 2009; Russell et al., 2010) and dSSA (e.g., Costabile et al., 2013; Li et al., 2015) were also used in different aerosol classification schemes. The SSA characterizes different aerosol types because values of ∼1 are typical of nonabsorbing "white aerosols" and values below 0.85 are associated with highly absorbing particles. Yang et al. (2009) combined the SSA values with corresponding SAE and AAE values to distinguish between desert dust, biomass burning, industrial plumes, and clean air in Beijing (China). Costabile et al. (2013) later proposed a scheme to classify aerosols based on the SAE, AAE, SSA, and dSSA using *in situ* urban data obtained over two years in Rome (Italy) coupled with numerical simulations to create a paradigm that links key aerosol populations to their unique aerosol optical properties. The developed paradigm is suitable to identify the presence of key aerosol populations including soot, biomass burning, organics, dust, and marine particles.

In this paper, nephelometer and aethalometer measurements were used to characterize the main extensive and intensive optical properties of PM2.5 particles that were monitored in winter (from December 2015 to March 2016) at a coastal site in southeastern Italy. Aerosol classification studies are generally performed by using ground-based remote sensing (e.g., Russell et al., 2010; Bahadur et al., 2012; Giles et al., 2012; Cazorla et al., 2013; Schmeisser et al., 2017) or satellite data (e.g., Russell et al., 2014). In contrast, ground-based in-situ measurements of aerosol optical properties were used in this study to identify and characterize different types of aerosols (e.g., Yang et al., 2009; Costabile et al., 2013; Cappa et al., 2016; Ealo et al., 2016; Pandolfi et al., 2018). The study area is affected by a large variety of aerosol types because of its geographic location in the center of the Mediterranean Basin. In particular, it is affected by mineral dust from the Sahara Desert and surrounding arid regions, polluted particles from urban and industrial areas of Northern and Eastern Europe, sea salt and spray from the Mediterranean Sea itself or from the Atlantic Ocean, and biomass-burning particles produced mostly in summer by forest fires (e.g., Perrone et al., 2012, 2014). Therefore, the performance of aerosol classification schemes with respect to the application to key particle and mixed aerosol populations was tested and their complex features were explored.

2. Experimental

2.1. Site description

The measurements of this study were performed at the Aerosol and Climate Laboratory of the Mathematics and Physics Department of the Salento University in Lecce (40.33°N, 18.11°E, 30 m a.s.l.) in southeastern Italy. The monitoring station is in a flat peninsular area, ∼6 km away from the city center of Lecce (∼95000 inhabitants), ∼20 km away from both the Ionian and Adriatic seas, and ∼100 and 800 km away from the Balkan and North African coasts, respectively. Therefore, it is representative of coastal sites of the Central Mediterranean, away from large sources of local pollution (e.g., Basart et al., 2009; Perrone et al., 2014).

2.2. Instrumentation

A light-emitting diode- (LED-)based integrating nephelometer (model Aurora 3000, ECOTECH, Knoxfield, Australia) was used to measure the aerosol scattering and backscattering coefficients (σ_s and β_s, respectively) at 450, 525, and 635 nm with a temporal resolution of 5 min. The nephelometer operates with the Kalman filter. Air was sampled from the top of a 1.5 m long stainless-steel tube with 15 mm internal diameter, which was equipped with a PM2.5 sampling head. A relative humidity threshold of 40% was set using a processor-controlled automatic heater inside the nephelometer to prevent hygroscopic effects that enhance particle scattering (e.g., Zieger et al., 2014, 2017; Titos et al., 2016). A full calibration of the device was carried out

approximately every two months using CO_2 as high span gas and internally filtered free air as low span gas. The precision was regularly checked (on a weekly basis) to detect any drift in the nephelometer calibration. Factors reported by Müller et al. (2011a) were used to correct systematic uncertainties due to angular truncation and non-Lambertian illumination. For a 5-min average time, the detection limits of the total aerosol scattering are 0.10, 0.13, and $0.11 \, Mm^{-1}$ at 450, 525, and 635 nm, respectively. The minimum values measured during this study were more than ten times larger than the corresponding detection limits.

An aethalometer model AE-31 (Magee Scientific, Berkeley, California, USA) equipped with a PM2.5 sampling head, separated from that of the nephelometer, was used to determine the aerosol absorption coefficient (σ_a) at seven wavelengths (370, 470, 520, 590, 660, 880, and 950 nm) with a temporal resolution of 5 min. The aethalometer AE-31 includes a quartz fiber filter tape: the air flow passes through it for a fixed temporal interval (5 min) at a constant flow rate ($\sim 4 \, l \, min^{-1}$). Due to the particle deposition on the filter tape, the radiation beam is attenuated for each of the seven wavelengths. The light attenuation at the 880 nm channel is considered standard for BC concentration calculations because other aerosol species do not exhibit absorption properties at this wavelength (Hansen et al., 1984). The attenuation coefficient σ_{aeth} can be directly estimated from aethalometer measurements, as reported in some studies (e.g., Weingartner et al., 2003; Arnott et al., 2005; Schmid et al., 2006). However, this parameter does not correspond to the aerosol absorption coefficient σ_a mainly because of measurement artifacts, as described in Collaud-Coen et al. (2010) who also summarized the main methodologies that were developed to convert σ_{aeth} data into aerosol absorption coefficients. In this study, we used the methodology recommended by the Aerosols, Clouds and Trace gases Research InfraStructure (ACTRIS; https://www.actris.eu), which was described by Müller (2015). For each wavelength λ, σ_a was derived from σ_{aeth} based on the following equation:

$$\sigma_a(\lambda) = \frac{\sigma_{aeth}(\lambda)}{C_0} \tag{1}$$

where C_0 (equal to 3.5 with an uncertainty of ± 25%) is the wavelength-independent correction factor empirically determined by Müller (2015). Aethalometer (e.g., Calvello et al., 2017; Saturno et al., 2017; Zotter et al., 2017), nephelometer (e.g., Perrone et al., 2014, 2015; Pandolfi et al., 2018), and both instruments (e.g., Ealo et al., 2016; Titos et al., 2017) have widely been used to monitor the aerosol light absorption and scattering coefficients at multiple wavelengths.

2.3. Particulate matter intensive optical parameters

The nephelometer operates at λ = 450, 525, and 635 nm, while the aethalometer operates at λ = 370, 470, 520, 590, 660, 880, and 950 (Section 2.2). The σ_a and σ_s values have been calculated at the aethalometer wavelengths to allow a proper comparison and calculate intensive parameters.

The SAE and AAE represent the spectral dependence of the scattering and absorption by particles, respectively, and can be estimated for the wavelength pair λ_1 = 470 nm and λ_2 = 660 nm using the following equations:

$$SAE(\lambda_1, \lambda_2) = -\frac{ln\left[\frac{\sigma_s(\lambda_1)}{\sigma_s(\lambda_2)}\right]}{ln\left(\frac{\lambda_1}{\lambda_2}\right)} \tag{2}$$

$$AAE(\lambda_1, \lambda_2) = -\frac{ln\left[\frac{\sigma_a(\lambda_1)}{\sigma_a(\lambda_2)}\right]}{ln\left(\frac{\lambda_1}{\lambda_2}\right)} \tag{3}$$

The SAE is an intensive optical parameter, which is strictly related to the aerosol size: particles with diameters larger than a few microns,

such as dust and sea salt aerosols, are characterized by SAE values below 1, while particles with diameters below 1 μm, such as anthropogenic particles, have SAE values larger than 1 (Seinfeld and Pandis, 1998; Schuster et al., 2006, and references therein). However, the SAE value alone does not provide unambiguous information on the relative weight of fine and coarse mode particles if both are present in the monitored air samples. In fact, Schuster et al. (2006) proved that large fine mode particles can have the same SAE as mixtures of coarse and small fine mode particles, indicating that it is also important to consider the wavelength pair used to calculate the SAE when qualitatively assessing the corresponding aerosol size distribution.

The AAE values provide information about the chemical composition of atmospheric aerosols (Ealo et al., 2016; Schmeisser et al., 2017) and can be used to evaluate the dominant absorbing aerosol type of a mixture of aerosols (Cazorla et al., 2013). The absorption by pure black carbon particles typically follows a λ^{-1} spectral dependence, yielding an AAE of ~ 1 (Bergstrom et al., 2002). Conversely, OC as BrC (e.g., Cappa et al., 2016; Costabile et al., 2017) and mineral dust contribute to light absorption mostly in the ultraviolet and blue spectral regions, yielding an AAE value larger than 1 (Kirchstetter et al., 2004; Kim et al., 2012). Collaud Coen et al. (2004), Petzold et al. (2009), and Yang et al. (2009) reported AAE values in the 1.5–6.5 range for mineral dust. The AAE values close to 1 may also be representative of urban pollution particles, while AAE values close to 2 are generally associated with biomass smoke particles including particles from wood burning in cities (Bergstrom et al., 2007; Russell et al., 2010; Clarke et al., 2007; Martinsson et al., 2015). Note that both the SAE and AAE values depend on the selected wavelength pair (Cazorla et al., 2013).

The SSA is defined as the ratio between σ_s and the extinction coefficient (equal to the sum of σ_s and σ_a) at a given wavelength λ:

$$SSA(\lambda) = \frac{\sigma_s(\lambda)}{\sigma_s(\lambda) + \sigma_a(\lambda)} \tag{4}$$

and represents the relative effect of scattering and absorption of the radiation. Therefore, it indicates the potential of aerosol particles to cool or warm the atmosphere (Haywood and Shine, 1995; Hansen et al., 1997; Bergstrom et al., 2007). The SSA varies from 0 for a completely absorbing or "black particle" to 1 for a purely scattering or "white particle" (Seinfeld and Pandis, 1998; Moosmüller et al., 2012). Therefore, nonabsorbing particles, such as sulfate, have a SSA of ~ 1, while lower SSA values (generally < 0.85) indicate the presence of more absorbing particles (Pandolfi et al., 2011). Hence, the SSA is widely used to characterize aerosol types (e.g., Russell et al., 2010, 2014; Gyawali et al., 2012). In this study, we also estimated the dSSA using the following equation:

$$dSSA(\lambda_1, \lambda_2) = SSA(\lambda_1) - SSA(\lambda_2) \tag{5}$$

Costabile et al. (2013) defined the dSSA as a type of "SSA Ångström exponent" because its value also depends on the aerosol size. Ackerman and Toon (1981) demonstrated that the predominance of coarse mode particles leads to positive dSSA values. Bergstrom (1973) reported negative dSSA values for aerosol mixtures that do not contain large mode particles. In fact, negative dSSA values were found for urban pollution and smoke aerosols (e.g., Dubovik et al., 2002; Bergstrom et al., 2007) and positive dSSA values were observed for desert dust (e.g., Kaufman et al., 2001; Müller et al., 2011b).

Schmeisser et al. (2017) provide a review on the classification schemes recently used to infer aerosol type from intensive optical properties. They found, in general, that the methodology to estimate the dominant aerosol type using optical properties was more suitable for monitoring sites with a stable and homogenous aerosol population, particularly continental polluted (carbonaceous aerosol), marine polluted (carbonaceous aerosol mixed with sea salt), and continental dust/biomass sites (dust and carbonaceous aerosol). However, the current classification schemes perform poorly when predicting dominant

aerosol type at remote marine and Arctic sites and at stations with more complex locations and topography where variable aerosol populations were not well represented by median optical properties. Therefore, more work is needed to find aerosol typing methods that are useful for a larger range of geographic locations and aerosol populations.

3. Aerosol optical properties: variability and daily trends

Several studies have been performed at the study site to characterize the aerosol optical and microphysical properties from remote sensing measurements (e.g., Perrone and Burlizzi, 2015; Perrone et al., 2015), the particle optical properties at the surface from nephelometer measurements (e.g., Perrone et al., 2014, 2015), and the particle chemical composition from *in situ* surface samplings (e.g., Perrone et al., 2013a, 2013b; Perrone et al., 2018). All studies have shown that the atmospheric particles over southeastern Italy are significantly affected by long-range transported particles from the surrounding countries and the Mediterranean Sea and that the study site could be considered representative of coastal sites of the Central Mediterranean away from large sources of local pollution. Then, lidar measurements have shown that the study site is characterized by a shallow (< 1000 m) planetary boundary layer (PBL), in accordance with radio sounding measurements (e.g., De Tomasi and Perrone, 2006; Perrone and Romano, 2018). The maximum value of the PBL height hourly mean is reached around midday and is equal to 470 ± 160 m in spring-summer (SS) and 580 ± 170 m in autumn-winter (AW). Therefore, it is on average greater in AW than in SS, in contrast to what is generally observed. A weak dependence of the PBL height on both the day hours and the seasons has also been observed, with respect to the ones generally observed worldwide (e.g., Seidel et al., 2012; Lewis et al., 2013), likely because of the site geographical location. Seidel et al. (2012) investigated the PBL climatology over the continental United States and Europe from radiosonde observations. They found that the median daytime PBL height was < 1 km over both continents, while median night-time values were < 0.5 km. Daytime values over Europe occasionally reached 2 km in summer. In contrast, 2 km-PBL-heights were more often found over the U.S. in both spring and summer. At the study site, the mean diurnal variation of the PBL height is of about 400 m in AW and 200 m in SS. The PBL height generally increased in the morning hours reaching the highest value around midday and, then, decreased with time because of the temperature and wind speed decrease (Perrone and Romano, 2018).

3.1. Scattering and absorption properties: main features and relationships

The main features of the scattering (σ_s) and absorption coefficient (σ_a) are presented and discussed in this subsection. Table 1 shows the main statistical parameters calculated both at 470 and at 660 nm based on hourly means. The σ_s (470 nm) mean value is slightly lower than that at 450 nm obtained from December 2011 to March 2012 (Perrone et al., 2014) for total suspended particles (TSP) likely because of the significant contribution of fine mode particles at the study site (e.g., Perrone et al., 2015; Donateo et al., 2018), if we assume that the aerosol sources affecting the study site have not significantly changed in the last five years. The mean σ_s and σ_a values are larger than the corresponding median values and, therefore, are characterized by a positively skewed distribution (Table 1).

Fig. 1a shows the daily evolution of the hourly averaged σ_s (black dots) and σ_a (grey triangles) values at 470 nm calculated by averaging all measurements from December 22, 2015, to March 30, 2016. Error bars represent the standard error of the mean (SEM). The σ_s and σ_a values are characterized by a similar daily trend, mainly driven by the wind speed (WS) as widely discussed in Perrone et al. (2015) for different seasons. Fig. 1d shows the daily evolution of the hourly averaged WS (black dots) and relative humidity (RH, grey triangles) at the surface from a local meteorological station. The PBL height generally

Table 1

Statistics (mean, standard deviation SD, median, minimum, maximum, and skewness values) of hourly averaged aerosol scattering and absorption parameters obtained from measurements performed from December 22, 2015, to March 30, 2016. The aerosol scattering and absorption coefficients (σ_s and σ_a, respectively) at 470 and 660 nm, aerosol scattering and absorption Ångström exponents (SAE and AAE, respectively) estimated for the wavelength pair 470–660 nm, single scattering albedo (SSA) at 470 and 660 nm, and single scattering albedo difference (dSSA) estimated for the wavelength pair 470–660 nm are reported.

Parameters	Mean	SD	Median	Min	Max	Skewness
σ_s (470 nm) [Mm^{-1}]	88	40	51	3	576	2.19
σ_s (660 nm) [Mm^{-1}]	54	25	34	2	383	2.94
σ_a (470 nm) [Mm^{-1}]	16	10	8	1	102	2.01
σ_a (660 nm) [Mm^{-1}]	10	6	5	1	67	2.12
SAE (470, 660 nm)	1.4	0.6	1.5	−0.7	3.0	−0.99
AAE (470, 660 nm)	1.5	0.3	1.4	0.6	3.4	0.99
SSA (470 nm)	0.83	0.09	0.86	0.30	0.99	−1.74
SSA (660 nm)	0.84	0.10	0.87	0.32	0.99	−1.53
dSSA (470, 660 nm)	0.00	0.07	0.00	−0.33	0.52	0.42

increases in the morning hours because of the heating of the Earth's surface, which in turn is mainly responsible for the decrease of the atmospheric stability and the related increase of WS and turbulent fluxes (Romano et al., 2017, 2018). The wind speed affects the vertical dispersion of the ground-level aerosols and, as a consequence, one observes that σ_s decreases (increases) with the increase (decrease) of WS. The σ_s daily evolution is also quite affected by the local temperature and relative humidity daily evolution, which is linked to the Sun's radiation reaching the Earth's surface. In fact, the mixing height and, hence, the vertical aerosol dispersion increase with the temperature, and the decrease of the relative humidity (Perrone and Romano, 2018). High ambient RHs favour chemical reactions leading to the formation of new atmospheric particles (Seinfeld and Pandis, 1998), besides affecting the size of hygroscopic aerosol components. Consequently, high ambient RHs may also affect the σ_s values. Therefore, the nighttime σ_s values are related to the lower PBL heights and WSs, which favour the accumulation of pollutants closer to the surface, to the emissions due to the vehicle traffic during the evening rush hours and the evening domestic heating, and likely to the high RHs. The early morning σ_s peak value is likely associated with the aerosols produced by the onset of anthropogenic activities, but it is contained by the wind speed rise. Results similar to the ones of Fig. 1 have also been found at Valencia (Spain), a coastal site of the western Mediterranean with a local meteorology rather similar to the one of this study (Esteve et al., 2012). Clear diurnal σ_s patterns were also observed at the urban site of Granada (Spain), where the morning σ_s peak values were, on average, reached later and were significantly larger than the evening σ_s peak values (Lyamani et al., 2010). Both the diurnal anthropogenic activities of the Granada urban area and the local meteorology were responsible for the diurnal σ_s pattern, according to Lyamani et al. (2010).

The daily σ_s and σ_a means are characterized by a large day-to-day variability due to the high variability of the particle types, properties, and concentrations. This effect could be attributed to the geographical location of the study site, which is also significantly affected by the contribution of long-range-transported particles, as discussed in several studies (e.g., Perrone et al., 2013a, 2014; 2015; Esteve et al., 2012). The hourly σ_a means are plotted as a function of the corresponding hourly σ_s means in Fig. 2, in addition to the fitting line, highlighting a significant spread of the data points. The Pearson correlation coefficient (R = 0.85), which is statistically significant with a p-value $\ll 0.01$, indicates that σ_a increases linearly with σ_s. Pandolfi et al. (2011) and Lyamani et al. (2008) reported similar relationships between σ_s and σ_a during measurement campaigns performed at two Mediterranean sites. Pandolfi et al. (2011) investigated the relationship between σ_s and σ_a in Montseny (Spain), a typical background site of the Western
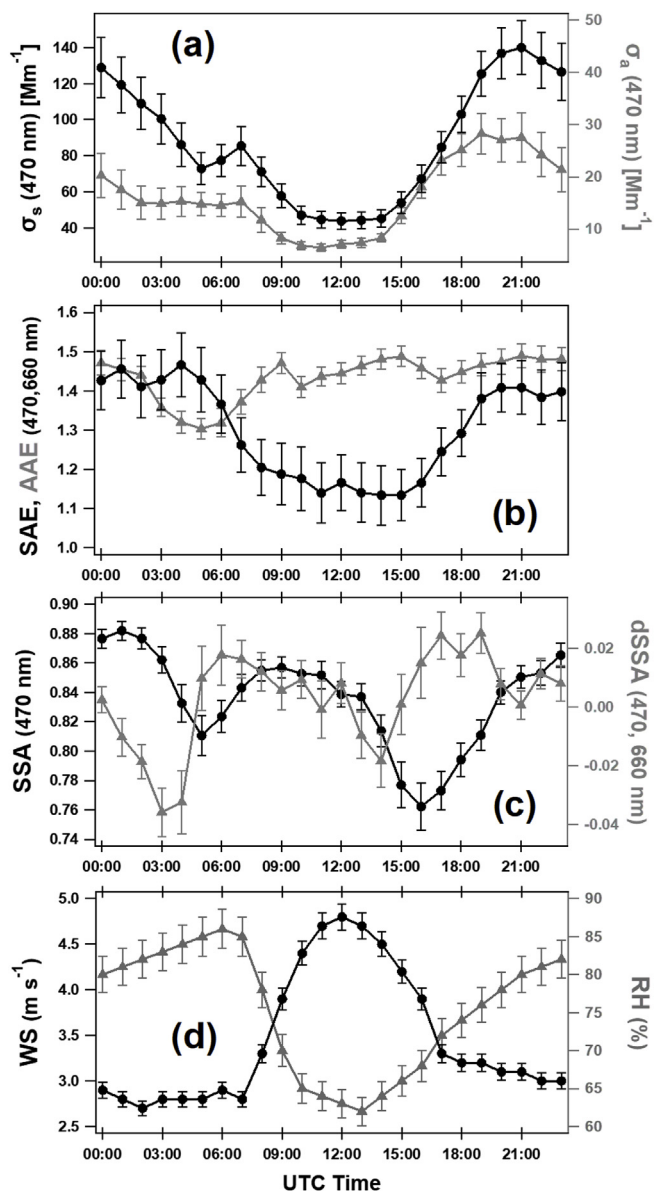
Fig. 1. Daily evolution of the hourly averaged aerosol (a) scattering coefficient (σ_s, black dots) and absorption coefficient (σ_a, grey triangles) at 470 nm, (b) scattering Ångström exponent (SAE, black dots) and absorption Ångström exponent (AAE, grey triangles) estimated for the wavelength pair 470–660 nm, (c) single scattering albedo (SSA, black dots) at 470 nm and single scattering albedo difference (dSSA, grey triangles) estimated for the wavelength pair 470–660 nm, and (d) wind speed (WS, black dots) and relative humidity (RH, grey triangles) from December 22, 2015, to March 30, 2016. The error bars represent the standard error of the mean.

Mediterranean area, and found that relatively high values of σ_s and σ_a were associated with a significant transport of anthropogenic particles at the study site. Lyamani et al. (2008) performed simultaneous absorption and scattering parameter measurements at an urban site in Granada, a non-industrialized and medium-sized city that is situated in a natural basin surrounded by mountains in southeastern Spain. During a specific pollution event, they found that the high values of both σ_s and σ_a were associated with air masses from Central Europe. In contrast, low σ_s and σ_a values were mainly associated with rain events or very high WS conditions.
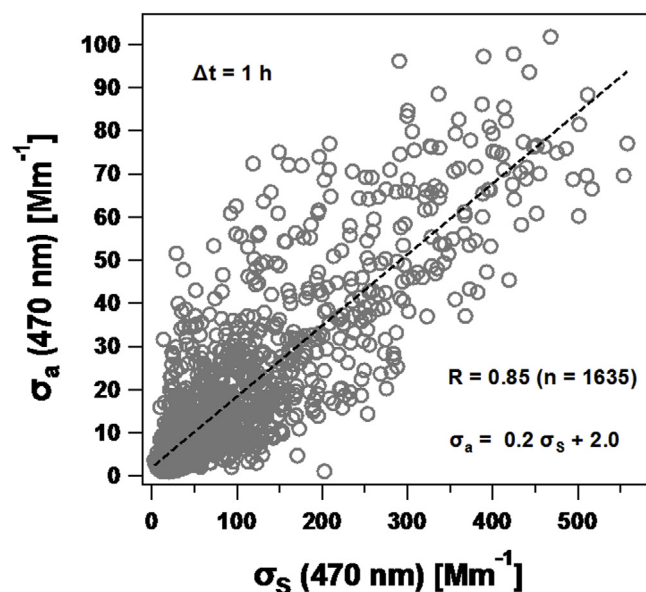

Fig. 2. Hourly mean aerosol absorption coefficients (σ_a, at 470 nm) as a function of the corresponding hourly mean aerosol scattering coefficients (σ_s, at 470 nm) from December 22, 2015, to March 30, 2016. The linear correlation coefficient (R), number of data points (n), and equation of the fitting regression line (dashed line) are also provided.

3.2. Intensive optical properties: main features and relationships

The main statistical parameters of SAE and AAE hourly means are reported in Table 1. The hourly SAE means vary from -0.7 to 3.0, with a mean value $\pm$ standard deviation (SD) of 1.4 ± 0.6. The SAE variability range and mean value are rather similar to the corresponding ones retrieved at the study site from TSP measurements performed from December 2011 to March 2012 (Perrone et al., 2014), likely because of the weak year-to-year variability of the aerosol mean properties and the dominance of fine mode particles (Perrone et al., 2015). The AAE hourly means range between 0.6 and 3.4, with a mean value ($\pm$ SD) of 1.5 ± 0.3. Note that this variability agrees with that observed by several authors for polluted aerosol particles and/or pollution mixed with natural aerosols in the Mediterranean Basin (e.g., Toledano et al., 2007; Costabile et al., 2013; Mallet et al., 2013). The mean AAE value is larger than the corresponding median value. The AAE values are therefore characterized by a positively skewed distribution. Conversely, the SAE values are characterized by a negatively skewed distribution, as also reported by Pandolfi et al. (2011).

Fig. 1b shows the daily evolution of the hourly averaged SAE (black dots) and AAE (grey triangles) values calculated by averaging all available measurements. The SAE values decrease with increasing WS at the surface (Fig. 1d) because fine mode particles are more efficiently dispersed than coarse ones, as discussed in Perrone et al. (2015). The hourly AAE means generally reach minimum values in the early morning, likely because of the increase of the fine-absorbing particle contribution, as also suggested by corresponding SAE values. The AAE values are in the range of 1.4–1.5 from approximately 09:00 UTC to midnight, without any marked dependence on the hour of the day.

Table 1 also reports the hourly-based statistics of the SSA at 470 and 660 nm and dSSA calculated for the 470–660 nm wavelength pair. The SSA values at 470 nm vary from 0.30 to 0.99, with a mean value ($\pm$ SD) of 0.83 ± 0.09, while dSSA values range from -0.33 to 0.52 with a mean value ($\pm$ SD) of 0.00 ± 0.07. The hourly SSA means are characterized by a negatively skewed distribution, as Pandolfi et al. (2011) also found. Conversely, the hourly dSSA means show a positively skewed distribution. The mean SSA value (at 470 nm; 0.83 ± 0.09, Table 1) estimated at the study site is consistent with the

mean value (0.76 ± 0.07) reported by Saha et al. (2008) for Toulon, an urban coastal site in southern France, based on data collected from December 2005 to February 2006. Mean SSA values similar to that of this study were also found at different Mediterranean coastal sites by Mallet et al. (2003), Gerasopoulos et al. (2003), and Pandolfi et al. (2011) and at the urban site of Granada (Spain) by Lyamani et al. (2010) and Titos et al. (2012).

Fig. 1c shows the mean daily evolution of the hourly averaged SSA at 470 nm (black dots) and dSSA (grey triangles) values (± SEM) and highlights that the SSA and dSSA values significantly vary depending on the hour of the day, unlike the AAE values. The hourly SSA means decrease in the first hours of the day, likely because of the increasing fine-absorbing particle contribution, as the SAE and AAE values also indicate (Fig. 1b). These values could be associated with aerosols dominated by fossil fuel and biomass burning particles, according to Bahadur et al. (2012). Then, the SSA values increase with increasing surface WS (Fig. 1d), which favors convective motions and, hence, the dispersion of fine mode particles that likely are the most absorbing particles. In fact, after midday, the mean SSA values decrease again with the decreasing WS because of the increasing fine-absorbing particle contribution at the surface. A similar diurnal variability was observed in an urban site by Lyamani et al. (2010) and it was attributed to an increase in the contribution of absorbing particles likely due to an increase of the anthropogenic activities. The hourly SSA means increase again after sunset, reaching nearly constant values at night. The hourly dSSA means also significantly vary depending on the hour of the day: the smallest and largest values are observed in the first hours of the day and around sunset, respectively. The daily dSSA trend appears to be linked to the daily evolution of local meteorological parameters (Fig. 1d). The smallest dSSA values that occur in the first hours of the day may also be associated with the increase of the fine-absorbing particles (Dubovik et al., 2002; Bergstrom et al., 2007). Conversely, the highest dSSA values that are generally observed from ~16:00 to 19:00 UTC (Fig. 1c, grey triangles) are likely due to a significant contribution of coarse mode particles as found by Ackerman and Toon (1981).

The ability of intensive parameters to distinguish among particles characterized by different absorption and scattering properties and, hence, of different type is further revealed by Fig. 3, which shows the 5-min mean values of the σ_s/σ_a ratio (at 470 nm) as a function of the corresponding dSSA values. The data points in Fig. 3 are color-coded by the corresponding 5-min average (a) SSA (at 470 nm) and (b) SAE (470 nm, 660 nm) values. Fig. 3a and b shows that the σ_s/σ_a, SSA, dSSA,
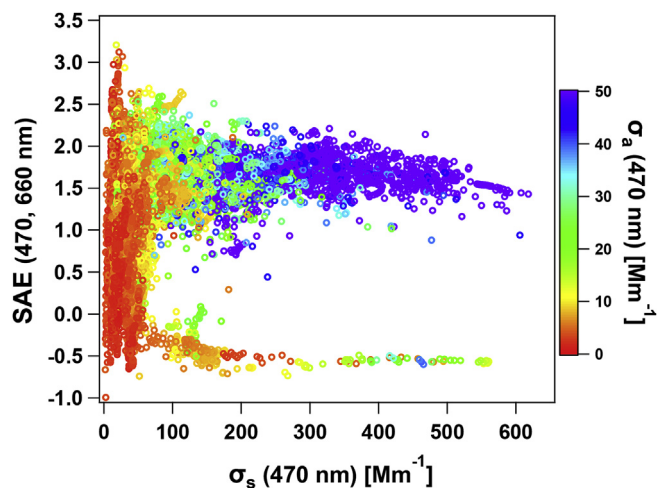

Fig. 4. Instantaneous (5 min) values of the scattering Ångström exponent (SAE, estimated for the wavelength pair at 470–660 nm) as a function of the corresponding aerosol scattering coefficients (σ_s, at 470 nm) and color-coded using the related values of the aerosol absorption coefficient (σ_a, at 470 nm). All instantaneous values from simultaneous nephelometer and aethalometer measurements from December 22, 2015, to March 30, 2016, were used. (For interpretation of the references to color in this figure legend, the reader is referred to the Web version of this article.)

and SAE values are spread over a wide range, likely because of the significant contribution of mixed particle populations at the study site. The σ_s/σ_a ratio increases with SSA (Fig. 3a) and 3b shows that the SAE variability range narrows and moves to smaller values with the increase of the σ_s/σ_a values, indicating that the highest σ_s/σ_a and SSA values are mainly associated with the large-size fraction of the monitored PM2.5 particles. Conversely, σ_s/σ_a and SSA values smaller than 5 and 0.75, respectively, can be associated with particle populations characterized by SAE values spanning the −0.5–2.5 range (Fig. 3a and b) and, hence, with both small- and large-size PM2.5 particles. Fig. 3b also shows that the dSSA values decrease with increasing SAE and, hence, with the decrease of the mean particle size. In more detail, Fig. 3b highlights that positive dSSA values are associated with particles and/or particle mixtures characterized by SAE values < 1 and that the dSSA assumes negative values for SAE values > 1.

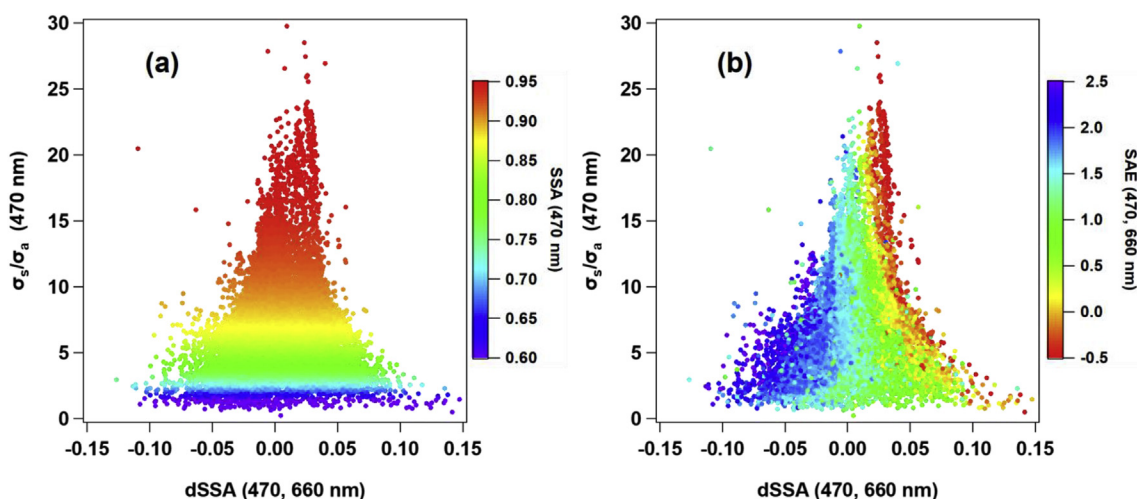Fig. 4 shows the 5-min average SAE values as a function of the

Fig. 3. Aerosol scattering to absorption coefficient ratio (σ_s/σ_a, at 470 nm) as a function of the single scattering albedo difference (dSSA, estimated for the wavelength pair at 470–660 nm) color-coded using the (a) single scattering albedo (SSA) at 470 nm and (b) scattering Ångström exponent (SAE) for the wavelength pair at 470–660 nm. All instantaneous values from simultaneous nephelometer and aethalometer measurements (with a temporal resolution of 5 min) from December 22, 2015, to March 30, 2016, were used. (For interpretation of the references to color in this figure legend, the reader is referred to the Web version of this article.)

corresponding σ_s values during the studied period. This type of graph is commonly used to identify different aerosol types (e.g., Santese et al., 2008). The data points in Fig. 4 are color-coded by the corresponding σ_a values. In addition to revealing the significant contribution of fine particles (particles with SAE > 1) at the study site, Fig. 4 also shows that the largest σ_s values are mainly associated with particles and/or particle mixtures characterized both by SAE values spanning approximately the 1.2–1.8 range and high σ_a values (> 30 Mm^{-1}). Conversely, situations characterized by a predominance of larger particles (SAE < 0.5) are associated with lower absorption and scattering coefficients. A similar behavior of the SAE as a function of σ_s was also reported by Pandolfi et al. (2011) for Montseny (Spain) and Aaltonen et al. (2006) for Pallas (Finland), a subarctic site at the northern border of the boreal forest zone. Aaltonen et al. (2006) observed the highest σ_s values (at 550 nm; > 40 Mm^{-1}) for SAE values in the 1.3–2.3 range by monitoring PM particles with aerodynamic diameters (d_{ae}) < 5 μm. The SAE was calculated for the 550–700 nm wavelength pair. They suggested that the high σ_s values were due to submicron particles from various combustion sources that were long-range-transported from Central or Eastern Europe rather than from local or regional pollution. Fig. 4 shows that quite high σ_s values (up to ~550 Mm^{-1}) associated with σ_a values up to ~40 Mm^{-1} were also observed for SAE values of approximately −0.5, representing an exception of the σ_s and σ_a decreasing trend for SAE values below 0.8. These last data points are mainly caused by the advection of dust particles from the Sahara Desert, characterized by both high scattering and absorbing properties, as it will be shown in the following discussion. In fact, Pandolfi et al. (2011) explained that the σ_s decreasing trend with decreasing SAE is mainly due to the absence of Saharan dust intrusions associated with negative SAE values and the prevalence of Atlantic advection episodes leading to low PM concentrations during their study period.

4. Identification of the main particle/particle mixture types

Graphical frameworks based on intensive optical parameters have generally been used to classify main particles using column (e.g., Bahadur et al., 2012; Giles et al., 2012; Cazorla et al., 2013) and surface aerosol properties (e.g., Costabile et al., 2013; Cappa et al., 2016), as discussed in Sections 1 and 3. We have tested several graphical frameworks and three examples of them have already been shown and discussed in Section 3.2 (Figs. 3 and 4). In the following subsection, we discuss the graphical framework that in our opinion allows to better define clusters of data points characterized by different intensive optical parameters and, hence, representative of different particle/particle mixture types.

4.1. Characterization of the selected classification scheme

We have found that a classification scheme based on the AAE vs. SAE plot (color-coded using the dSSA) can represent one of the best graphical frameworks involving optical parameters that can be used to discriminate between different PM2.5 particle/particle mixture types at the study site. Because the SAE is strictly related to the mean aerosol size and the AAE provides information on both the aerosol composition and size, the combination of these two intensive optical parameters allows to infer the aerosol types (Costabile et al., 2017; Cappa et al., 2016, and references therein). In addition, the dSSA, which characterizes the spectral dependence of the SSA, can be used to clearly separate the optical data in a graphical framework with respect to other intensive parameters, based on Costabile et al. (2013). They highlighted that this last result is mainly associated with both the inverse correlation between SAE and dSSA, resulting from their common dependence on the particle size (clearly shown in Fig. 3b), and the inverse correlation between AAE and dSSA, determined by their common dependence on the particle composition. Russell et al. (2010) also used the dSSA to classify the main particle types.
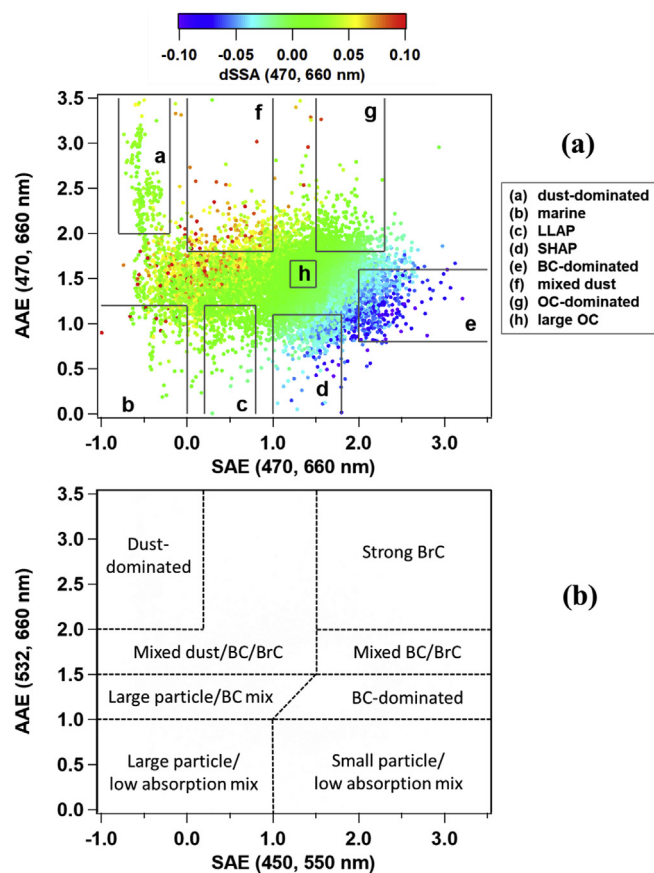

Fig. 5. (a) Instantaneous (5 min) absorption Ångström exponents (AAEs, at the wavelength pair 470–660 nm) as a function of the corresponding scattering Ångström exponents (SAEs, at the wavelength pair 470–660 nm), color-coded using the related single scattering albedo difference (dSSA, at the wavelength pair 470–660 nm). All instantaneous values from simultaneous nephelometer and aethalometer measurements from December 22, 2015, to March 30, 2016, were used. The grey boxes represent the eight selected clusters: (a) dust-dominated, (b) marine, (c) large and low-absorbing particles (LLAP), (d) small and high-absorbing particles (SHAP), (e) black carbon (BC)-dominated, (f) mixed dust, (g) organic carbon (OC)-dominated, and (h) large OC particles. The dashed black lines in (b) represent the classification scheme from Cappa et al. (2016). (For interpretation of the references to color in this figure legend, the reader is referred to the Web version of this article.)

Fig. 5a shows the 5-min average AAE values as a function of the corresponding SAE values, color-coded using the dSSA values. The three intensive parameters were evaluated for the 470–660 nm wavelength pair. For comparison, Fig. 5b represents the classification scheme based on the relationship between AAE and SAE proposed by Cappa et al. (2016), where the AAE and SAE values were calculated for the 532–660 nm and 450–550 nm wavelength pair, respectively. Cappa et al. (2016) delineated the whole AAE vs. SAE framework area and categorized all combinations of optical property values, as shown in Fig. 5b. They particularly classified particles with 1 < AAE < 1.5 and SAE > 1 as black carbon (BC) dominated (BC is approximately equivalent to EC; Lack et al., 2014). Particles with AAE > 2 and SAE > 1.5 were considered to be absorbing OC or strong BrC. Dust-dominated particles were associated with AAE > 2 and SAE < 0.5. The other sectors of the graphical framework from Cappa et al. (2016) were associated with specific particle mixtures. The comparison of Fig. 5a and b shows that the AAE and SAE values in this study are within the variability ranges suggested by Cappa et al. (2016) and that the optical parameters continuously vary within the identified ranges because of the high variability of the particle/particle mixture types. The geographical location of the study site in the Central Mediterranean Basin

contributes to these last results (e.g., Perrone et al., 2013a, 2014, 2015), as mentioned.

The AAE and SAE values in this study were calculated for wavelength pairs different from those by Cappa et al. (2016) because different instruments were used. The AAE (470 nm, 660 nm) and SAE (470 nm, 660 nm) values were on average 12% smaller and 29% greater, respectively, than the corresponding AAE (532 nm, 660 nm) and SAE (450 nm, 550 nm) values because of the dependence of the AAE and SAE values on the selected wavelength pair. Figs. S1a and b in the Supplementary Material provide the plots of AAE (470 nm, 660 nm) versus AAE (532 nm, 660 nm) and SAE (470 nm, 660 nm) versus SAE (450 nm, 550 nm), respectively.

We observed that the AAE versus SAE plot color-coded using the dSSA values (Fig. 5a) allows a better identification of different particle/particle mixture types than the corresponding plot color-coded using the SSA values. The weaker dependence of the AAE–SAE relationship on SSA values is likely responsible for this last result. For comparison, Fig. S2 in the Supplementary Material shows the 5-min average AAEs versus the corresponding SAEs, color-coded using the SSA values. Fig. S2 shows that the SSA values on average increase with the decrease of the SAE values and highlights a rather weak dependence of SSA on the AAE values.

Fig. 5a shows that on average the AAE increases with the SAE decrease, mainly for negative SAE values that are associated to large-size particles as desert dust. The dSSA (470 nm, 660 nm) on average decreases with increasing SAE (470 nm, 660 nm) because negative dSSA values are linked to larger SSAs at 660 nm by anthropogenic pollution particles containing BC, as mentioned before. Conversely, positive dSSA values are associated with larger SSAs at 470 nm by mineral dust containing iron oxide.

The smooth and continuous variability of the AAE, SAE, and dSSA values within their corresponding variability range resulting from Fig. 5a is likely due to the different degrees of mixing of particles of various type. We believe that clusters of data points related to specific aerosol and/or aerosol mixture types can likely be identified at the edges of the graphical framework area where data points are located (Fig. 5a). The highest and/or the smallest values of the plotted intensive parameters fall in the above mentioned edge areas and they are likely more suitable to identify aerosol populations of a specific type, as it will be shown in the following. The grey boxes in Fig. 5a identify the variability ranges of the AAE, SAE, and dSSA values that we have selected to investigate the mean features of different particle/particle mixture types. Table 2 shows the variability of the SAE, AAE, and dSSA values, in addition to the corresponding SSA (470 nm) ranges, which have been used to identify eight different clusters of data points (denoted by the letters a–h in Fig. 5a). Results from previous studies and the aerosol classification scheme from Cappa et al. (2016) reported in Fig. 5b have also been accounted for to select the variability ranges of the intensive optical parameters related to the grey boxes of Fig. 5a. However, it is worth observing that they are not the only possibilities of

classification because of the smooth and continuous changes of all intensive parameters at the study site.

The dust-dominated particles (cluster a) are characterized by negative SAE values (-0.8 to -0.2) because of their large mean size and by AAE values in the range of 2.0–3.5 based on previous studies (e.g., Collaud Coen et al., 2004; Yang et al., 2009). The corresponding SSA and dSSA values vary within the 0.87–0.99 and 0.01–0.07 ranges, respectively, because of the small absorption coefficients and the decreasing trend of the SSA depending on the wavelength for desert dust particles (e.g., Müller et al., 2011b, and references therein). Negative SAE values (-1–0) are also assigned to marine particles (cluster b) because of the significant contribution of their large size (Seinfeld and Pandis, 1998). The corresponding SSA and dSSA values vary in the ranges 0.85–0.99 and -0.01–0.08, respectively, which are in reasonable accordance with the findings by Costabile et al. (2013). In fact, SSA values close to one and dSSA values close to zero are assigned to marine particles because of their low absorbing properties and the weak spectral dependence of the SSA (Dubovik et al., 2002; Russell et al., 2010; and references therein) in the wavelength range of this study. The AAE range of marine particles is poorly defined in the literature. Indeed, Russell et al. (2010) emphasized that the AAE used as an indicator of the aerosol composition is not applicable to pure sea salt particles because of undefined AAE values. Moreover, according to Schmeisser et al. (2017), a major missing piece of currently available aerosol classification methods is the identification and validation of optical property thresholds to classify sea salt particles. The AAE values of marine particles vary in the range 0.0–1.5 based on the classification scheme used in this study, which is also supported by the discussion in Section 5. Note that the Positive Matrix Factorization (PMF) technique applied to chemically speciated PM2.5 samples collected at the study site from July 2008 to May 2010 clearly indicated a secondary marine source characterized by Na^+ and Cl^- as principal markers (Perrone et al., 2013b).

The AAE values ranging from 0.0 to 1.2 are also assigned to the aerosol mixture made by large and low absorbing particles (LLAP, cluster c), characterized by $0.2 < SAE < 0.8$ and $0.00 < dSSA < 0.06$. Marine and anthropogenic pollution particles likely contributed to the LLAP mixture. The SSA variability (0.70–0.96) supports this last assumption. Conversely, the contribution of fine and absorbing particles increases with increasing SAE, mainly for AAE < 1, as shown in Fig. 5a. Therefore, the cluster d characterized by $0.0 < AAE < 1.1$, $1.0 < SAE < 1.8$, and $-0.09 < dSSA < 0.00$ has been selected to represent a particle mixture consisting of small and high-absorbing particles (SHAP), indicating a significant contribution of BC particles. The SSA variability (0.40–0.89) and negative dSSA values likely support the main features of cluster d. The BC-dominated cluster e is characterized by $0.8 < AAE < 1.6$, $2 < SAE < 3.5$, $-0.10 < dSSA < -0.02$, and $0.39 < SSA < 0.85$, which agrees with the results by Cappa et al. (2016).

Mineral dust and OC contribute to light absorption, mostly in the

Table 2

Variability of the intensive aerosol optical properties (scattering Ångström exponent SAE and absorption Ångström exponent AAE for the wavelength pair at 470–660 nm, single scattering albedo SSA at 470 nm, and single scattering albedo difference dSSA for the wavelength pair at 470–660 nm) and number (N) of experimental data related to the eight selected clusters: (a) dust-dominated, (b) marine, (c) large and low-absorbing particles (LLAP), (d) small and high-absorbing particles (SHAP), (e) black carbon (BC)-dominated, (f) mixed dust, (g) organic carbon (OC)-dominated, and (h) large OC particles.

Cluster	SAE (470, 660 nm)	AAE (470, 660 nm)	SSA (470 nm)	dSSA (470, 660 nm)	N
(a) dust-dominated	-0.8–-0.2	2.0–3.5	0.87–0.99	0.01–0.07	179
(b) marine	-1–0	0.0–1.2	0.85–0.99	-0.01–0.08	152
(c) LLAP	0.2–0.8	0.0–1.2	0.70–0.96	0.00–0.06	255
(d) SHAP	1.0–1.8	0.0–1.1	0.40–0.89	-0.09–0.00	438
(e) BC-dominated	2.0–3.5	0.8–1.6	0.39–0.85	-0.10–-0.02	459
(f) mixed dust	0–1	1.8–3.5	0.57–0.97	-0.01–0.09	213
(g) OC-dominated	1.5–2.3	1.8–3.5	0.67–0.95	-0.03–0.05	355
(h) large OC	1.2–1.5	1.4–1.7	0.66–0.96	-0.01–0.03	705

ultraviolet and blue spectral regions, yielding AAE values larger than 1 (Schmeisser et al., 2017; and references therein). Consequently, the clusters f and g in Fig. 5a are representative of mixtures that are largely affected by dust particles (mixed dust cluster) and absorbing OC particles (OC-dominated cluster), respectively. The SSA and the dSSA ranges (0.57–0.97 and −0.01–0.09, respectively) suggest that the mixed dust cluster was also affected by absorbing OC particles, which are characterized by similar SSA and dSSA values (0.67–0.95 and −0.03–0.05, respectively). Therefore, the clusters f and g are representative of the "reacted dust" and "combustion including biomass burning" sources, respectively, identified by the PMF technique applied to chemically speciated PM2.5 particles (Perrone et al., 2013b). The cluster h in Fig. 5a represents a mixture dominated by OC particles. The SAE variability (1.2–1.5) indicates that the particle mean size of cluster h is greater than that of cluster g. Consequently, this cluster was denoted as "large OC". The related AAE variability also highlights the differences between the OC-dominated and large-OC mixtures. It is well known that the OC particles include primary and secondary components (POC and SOC, respectively). In a recent study, Perrone et al. (2018) showed that the POC contribution decreases with the decrease of the mean SAE value. Consequently, we assume that the larger contribution of the SOC particles to cluster h than to cluster g is likely responsible for the different optical parameters characterizing the two clusters.

The frequency distribution of the (a) SSA, (b) SAE, (c) AAE, and (d) dSSA values associated with the identified particle/particle mixture types are shown in Fig. S3 of the Supplementary Material to highlight the SSA weak ability to identify different particle/particle mixture types and show that SAE, AAE, and dSSA are more suitable parameters, even if one must be aware that the frequency distributions are biased by the classification scheme that limits the SAE and AAE value of each cluster.

The 5-min average SAE values of the eight selected clusters (Fig. 5a) marked by different colors/symbols have been plotted in Fig. 6 as a function of the corresponding σ_s values at 470 nm to highlight how the identified particle/particle mixture types affect an extensive parameter such as σ_s and, hence, provide further insight into the loading of the different particle types. Schmeisser et al. (2017) explained that the incorporation of aerosol extensive parameters into a classification scheme based on intensive optical parameters leads to a more complete picture of the aerosol type and conditions at the monitoring station. However, to the best of our knowledge, very few studies have made use of extensive optical properties to support the identified particle/particle mixture types at particular sites (e.g., Schmeisser et al., 2017, and references therein). Undefined data points are marked by grey open dots in Fig. 6. The identified particle/particle mixture types are generally located in different regions of the SAE vs. σ_s framework, highlighting their different impact on the analyzed extensive parameter. Interestingly, Fig. 6 shows that the clusters b, c, and f, typically dominated by large-size particles, are generally responsible for the lowest σ_s values. Conversely, the highest σ_s values are associated with dust particles (cluster a) and mainly with cluster d, which is representative of particle mixtures dominated by BC. The OC-dominated (cluster g) and the large OC mixture (cluster h) are also responsible for high σ_s values. Fig. 6 highlights the significant role of the OC and BC particle mixtures with respect to other species that are characterized by SAE < 1 because of their high σ_s values. These last findings are supported by mass reconstruction analyses of chemically-speciated PM2.5 samples, which showed that the organic matter and BC mass represent nearly 58% of the PM2.5 total mass (Perrone et al., 2013b).

4.2. Case studies: main features of dust-dominated, BC-dominated, and marine particles

The temporal evolutions of intensive and extensive optical parameters of most particles associated with clusters a, b, and e (Fig. S4 in the Supplementary Material) are analyzed in this section with the main
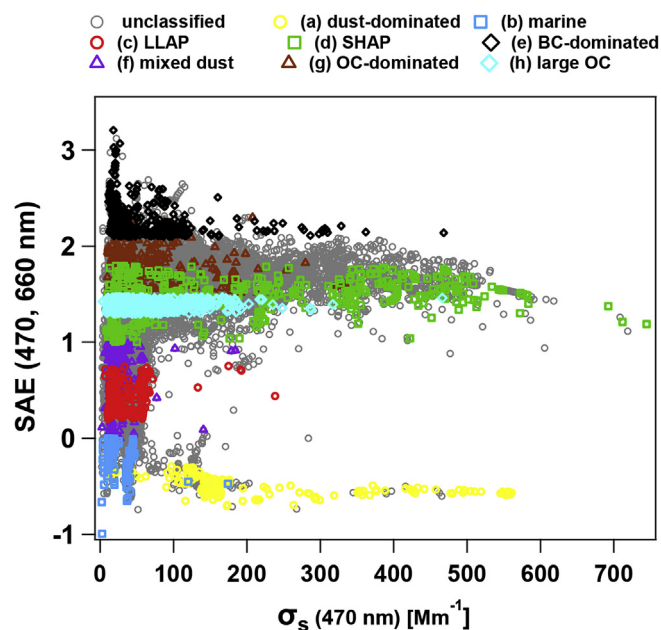

Fig. 6. Instantaneous (5 min) scattering Ångström exponents (SAEs, for the wavelength pair at 470–660 nm) as a function of the corresponding aerosol scattering coefficients (σ_s, at 470 nm) from December 22, 2015, to March 30, 2016, for the eight selected clusters: dust-dominated (yellow circles), marine (blue boxes), large and low-absorbing particles (LLAP, red circles), small and high-absorbing particles (SHAP, green boxes), black carbon (BC)-dominated (black diamonds), mixed dust (violet triangles), organic carbon (OC)-dominated (brown triangles), and large OC particles (light blue diamonds). The grey circles represent unclassified data, which do not belong to a specific cluster. (For interpretation of the references to color in this figure legend, the reader is referred to the Web version of this article.)

goal of further demonstrating the ability of the selected aerosol classification scheme to detect different particle types. Table 3 shows the measurement days and the corresponding time intervals during which most of the data points (more than 87%) of cluster a, b, and e were retrieved. Most of cluster-a particles (> 97%) were monitored during the February 28–29, 2016 dust event (Fig. S5, Supplementary Material) and the severe dust outbreak that affected southern Italy on March 22–23, 2016 (e.g., Rizza et al., 2018), as the back trajectory pathways from the HYbrid Single-Particle Lagrangian Integrated Trajectory (HYSPLIT) model also show (Fig. S6, Supplementary Material). The comparison of Table 3 data with the corresponding ones of Table 1 shows that the dust-dominated σ_s values of March 22–23 are significantly greater than the corresponding mean values retrieved throughout the sampling period (Table 1). The SAE and AAE mean values of the dust-dominated particles (Table 3) are significantly smaller and greater, respectively, than the corresponding mean values reported in Table 1 because of the large mean size of mineral dust particles and their light absorption mostly in the ultraviolet and blue spectral regions (e.g., Kirchstetter et al., 2004; Kim et al., 2012), respectively. Consequently, the dSSA values of dust-dominated particles are greater than the corresponding Table 1 mean value.

Most (> 91%) of the marine particles (cluster b) were monitored on 5 different days of February and March 2016 (Table 3). In fact, the back trajectory pathways show that the air masses crossed the Mediterranean Sea at very low altitudes before reaching the study site (Fig. S7) and were likely responsible for the advection of marine particles. The marine σ_s mean values are smaller than the corresponding mean value of the whole study period (Table 1) because of the low particle concentration, as commonly observed during the advection of marine aerosols (e.g., Perrone et al., 2015), and/or the particle shape and size. The marine SAE and AAE mean values (Table 3) are smaller than the

Table 3

Measurement days and corresponding time intervals during which most of the data points related to the cluster a (dust-dominated), cluster b (marine), and cluster e (BC-dominated) were retrieved. The corresponding mean values of scattering and absorption Ångström exponents (SAEs and AAEs, respectively) for the wavelength pair at 470–660 nm, single scattering albedo difference (dSSA) for the wavelength pair at 470–660 nm, and aerosol scattering coefficient (σ_s) at 470 nm related to the selected intervals have been also reported.

Cluster	Start Time (dd/mm/yy; UTC time)	End Time (dd/mm/yy; UTC time)	SAE (470, 660 nm)	AAE (470, 660 nm)	dSSA (470, 660 nm)	σ_S (470 nm) [Mm^{-1}]
a (dust-dominated)	28/02/16; 23:15	29/02/16; 05:15	−0.53	2.30	0.03	141
	22/03/16; 16:05	23/03/16; 07:40	−0.50	2.68	0.03	254
b (marine)	13/02/16; 05:20	13/02/16; 11:45	−0.26	1.10	0.07	12
	15/02/16; 21:40	16/02/16; 04:45	−0.35	1.05	0.03	38
	05/03/16; 20:20	06/03/16; 04:15	−0.09	1.06	0.02	19
	12/03/16; 04:10	12/03/16; 08:30	−0.14	0.99	0.03	16
	13/03/16; 01:40	13/03/16; 05:05	−0.21	0.85	0.05	11
e (BC-dominated)	23/12/15; 21:50	24/12/16; 06:15	2.19	1.30	−0.04	170
	04/01/16; 00:30	04/01/16; 07:05	2.11	1.35	−0.05	83
	19/01/16; 10:55	20/01/16; 15:40	2.41	1.31	−0.05	85
	23/01/16; 08:35	23/01/16; 15:15	2.07	1.36	−0.03	27
	25/01/16; 09:00	25/01/16; 16:25	2.17	1.14	−0.06	34
	06/02/16; 00:30	06/02/16; 15:30	2.33	1.31	−0.05	18
	11/02/16; 19:30	12/02/16; 06:25	2.12	1.46	−0.04	90

corresponding mean values of the total sampling period because of the predominance of large-size particles. Consequently, the marine dSSA mean values are on average greater than the corresponding mean value reported in Table 1.

Most (> 83%) of the BC-dominated particles (cluster e) were monitored on 7 different time intervals (Table 3) likely affected by severe pollution events. In fact, the HYSPLIT back trajectory pathways show that the related air masses crossed northern European countries, likely affected by anthropogenic pollution, before reaching the study site (Fig. S8). Several studies showed that advection patterns similar to those of Fig. S8 were responsible for the transport of fine mode particles mainly due to traffic and combustion including biomass-burning sources at the study site (e.g., Perrone et al., 2013a, 2014). The BC-dominated σ_s mean values (Table 3) are smaller, similar, or greater than the corresponding σ_s mean value reported in Table 1, likely because of the change of the BC-particle amount with the monitoring day. In fact, the SAE and dSSA mean values (Table 3) are on average greater and smaller, respectively, than the corresponding mean value of the whole sampling period because of the predominance of fine absorbing particles. Note that negative dSSA values were generally found for urban pollution and smoke aerosols (e.g., Dubovik et al., 2002; Bergstrom et al., 2007). The AAE values of the BC-dominated particles (Table 3) vary within the range of the corresponding mean value reported in Table 1.

In conclusion, we believe that Table 3 supports the used classification, in addition to revealing the high variability of the particle optical properties.

5. Summary and conclusion

Multiwavelength nephelometer and aethalometer measurements were analyzed with the main goal of defining a graphical framework based on intensive optical parameters (σ_s/σ_a, SAE, AAE, SSA, and dSSA) that can be used to identify different particle/particle mixture types. Both the nephelometer and the aethalometer were equipped with a PM2.5 sampling head and the respective measurements were performed at the surface of a coastal site of the Central Mediterranean Basin affected by long-range contributions from surrounding countries. Consequently, both the extensive and the intensive particle parameters vary smoothly and continuously within their respective ranges, which are similar to those observed at other Mediterranean coastal sites.

- The plot of the σ_a hourly means as a function of the corresponding σ_s

hourly means shows that most of the absorbing particles are also responsible for high scattering coefficients. Then, the SAE values point out that the highest σ_a and σ_s values are on average associated with the fine fraction of the PM2.5 sampled particles. In contrast, the large-size PM2.5 particles (SAE < 0.5) are on average responsible for small σ_a and σ_s values.
- The SAE variability range narrows and moves to smaller values with the increase of the σ_s/σ_a and SSA values, indicating that the highest σ_s/σ_a and SSA values are mainly associated with the large-size PM2.5 particles. Conversely, σ_s/σ_a and SSA values smaller than 5 and 0.75, respectively, are associated with particle populations characterized by SAE values spanning the −0.5–2.5 range because of the contribution of both small- and large-size PM2.5 particles.
- The σ_s/σ_a versus dSSA plot color-coded using the related SAE values shows that the dSSA values decrease with increasing SAE showing that the particle populations with SAEs > 1.5 and, hence, associated with the smallest particles in the PM2.5 fraction, are characterized by negative dSSAs.
- The AAE versus SAE plot, color-coded using the corresponding dSSA values, is considered to represent the best framework for the identification of different particle/particle mixture types.
- The results also show that marine, LLAP, and mixed dust clusters, all characterized by SAE values below 1, are responsible for σ_s values (at 470 nm) smaller than 100 Mm^{-1}. On the contrary, the SHAP, BC-dominated, and OC-based mixtures are on average responsible for the highest σ_s values and are the dominant particle species.
- The SAE, AAE, and dSSA ranges were selected with the main goal of highlighting the specific features of the main identified particles/particle mixtures, but they are not the only possibilities of classification because of the smooth and continuous changes of all intensive parameters at the study site.
- The ability of the used classification scheme to identify particles of different type also results from the analysis of most of the data points associated with the dust-dominated, marine, and BC-dominated cluster. In fact, we have verified that they refer to measurements performed on days affected by air masses that crossed northern Africa, the Mediterranean Sea, and the anthropogenic polluted regions of northern and eastern Europe, respectively, before reaching the monitoring site.

In conclusion, this paper contributes to the characterization of the PM2.5 fraction optical properties over the Central Mediterranean area and, consequently, can be considered of general interest. This paper

also shows that the smooth and continuous changes of all intensive parameters do not allow to uniquely identify different types of particles because of the contribution of natural and anthropogenic particles from local sources and/or particles long-range-transported to the study site from surrounding countries.

Acknowledgments

Appendix A. Supplementary data

Supplementary data to this article can be found online at https://doi.org/10.1016/j.atmosenv.2019.01.037.

References

Aaltonen, V., Lihavainen, H., Kerminen, V.M., Komppula, M., Hatakka, J., Eneroth, K., Kulmala, M., Visanen, Y., 2006. Measurements of optical properties of atmospheric aerosols, in Northern Finland. Atmos. Chem. Phys. 6, 1155–1164. https://doi.org/10.5194/acp-6-1155-2006.

Ackerman, P., Toon, O.B., 1981. Absorption of visible radiation in atmosphere containing mixtures of absorbing and nonabsorbing particles. Appl. Opt. 20, 3661–3668. https://doi.org/10.1364/AO.20.003661.

Andreae, M.O., Gelencsér, A., 2006. Black carbon or brown carbon? The nature of light-absorbing carbonaceous aerosols. Atmos. Chem. Phys. 6, 3131–3148. https://doi.org/10.5194/acp-6-3131-2006.

Arnott, W., Hamasha, K., Moosmüller, H., Sheridan, P., Ogren, J., 2005. Towards aerosol light-absorption measurements with a 7-wavelength Aethalometer: evaluation with a photoacoustic instrument and 3-wavelength nephelometer. Aerosol Sci. Technol. 39, 17–29. https://doi.org/10.1080/027868290901972.

Bahadur, R., Praveen, P.S., Xu, Y., Ramanathan, V., 2012. Solar absorption by elemental and brown carbon determined from spectral observations. Proc. Natl. Acad. Sci. U.S.A. 109 (43), 17366–17371. https://doi.org/10.1073/pnas.1205910109.

Basart, S., Pérez, C., Cuevas, E., Baldasano, J.M., Gobbi, G.P., 2009. Aerosol characterization in northern Africa, northeastern Atlantic, Mediterranean Basin and Middle East from direct-sun AERONET observations. Atmos. Chem. Phys. 9, 8265–8282. https://doi.org/10.5194/acp-9-8265-2009.

Bergstrom, R.W., 1973. Extinction and absorption coefficients of the atmospheric aerosol as a function of particle size. Beitr. Phys. Atmos. 46, 223–234.

Bergstrom, R.W., Russell, P.B., Hignett, P., 2002. Wavelength dependence of the absorption of black carbon particles: predictions and results from the TARFOX experiment and implications for the aerosol single scattering albedo. J. Atmos. Sci. 59, 567–577. https://doi.org/10.1175/1520-0469(2002)059<0567:WDOTAO>2.0.CO;2.

Bergstrom, R.W., Pilewskie, P., Russell, P.B., Redemann, J., Bond, T.C., Quinn, P.K., Sierau, B., 2007. Spectral absorption properties of atmospheric aerosols. Atmos. Chem. Phys. 7, 5937–5943. https://doi.org/10.5194/acp-7-5937-2007.

Calvello, M., Caggiano, R., Esposito, F., Lettino, A., Sabia, S., Summa, V., Pavese, G., 2017. IMAA (Integrated Measurements of Aerosol in Agri valley) campaign: multi-instrumental observations at the largest European oil/gas pre-treatment plant area. Atmos. Environ. 169, 297–306. https://doi.org/10.1016/j.atmosenv.2017.09.026.

Cappa, C.D., Kolesar, K.R., Zhang, X., Atkinson, D.B., Pekour, M.S., Zaveri, R.A., Zelenyuk, A., Zhang, Q., 2016. Understanding the optical properties of ambient sub- and supermicron particulate matter: results from the CARES 2010 field study in northern California. Atmos. Chem. Phys. 16, 6511–6535. https://doi.org/10.5194/acp-16-6511-2016.

Cazorla, A., Bahadur, R., Suski, K.J., Cahill, J.F., Chand, D., Schmid, B., Ramanathan, V., Prather, K.A., 2013. Relating aerosol absorption due to soot, organic carbon, and dust to emission sources determined from in-situ chemical measurements. Atmos. Chem. Phys. 13, 9337–9350. https://doi.org/10.5194/acp-13-9337-2013.

Charlson, R.J., Schwartz, S.E., Hales, J.M., Cess, R.D., Coakley, J.A., Hansen, J., Hofmann, D.J., 1992. Climate forcing by anthropogenic aerosols. Science 255, 423–430. https://doi.org/10.1126/science.255.5043.423.

Chin, M., Diehl, T., Ginoux, P., Malm, W., 2007. Intercontinental transport of pollution and dust aerosols: implications for regional air quality. Atmos. Chem. Phys. 7, 5501–5517. https://doi.org/10.5194/acp-7-5501-2007.

Clarke, A., McNaughton, C., Kapustin, V., Shinozuka, Y., Howell, S., Dibb, J., Zhou, J., Anderson, B., Brekhovskikh, V., Turner, H., Pinkerton, M., 2007. Biomass burning and pollution aerosol over North America: organic components and their influence on spectral optical properties and humidification response. J. Geophys. Res. 112, D12S18. https://doi.org/10.1029/2006JD007777.

Coakley, J.A., Cess, R.D., Yurevich, F.B., 1983. The effect of tropospheric aerosols on the Earth's radiation budget: a parameterization for climate models. J. Atmos. Sci. 40, 116–138. https://doi.org/10.1175/1520-0469(1983)040<0116:TEOTAO>2.0.CO;2.

Collaud Coen, M., Weingartner, E., Schaub, D., Hueglin, C., Corrigan, C., Henning, S., Schwikowski, M., Baltensperger, U., 2004. Saharan dust events at the Jungfraujoch: detection by wavelength dependence of the single scattering albedo and first climatology analysis. Atmos. Chem. Phys. 4, 2465–2480. https://doi.org/10.5194/acp-4-2465-2004.

Collaud Coen, M., Weingartner, E., Apituley, A., Ceburnis, D., Fierz-Schmidhauser, R., Flentje, H., Henzing, J.S., Jennings, S.G., Moerman, M., Petzold, A., Schmid, O., Baltensperger, U., 2010. Minimizing light absorption measurement artifacts of the Aethalometer: evaluation of five correction algorithms. Atmos. Meas. Tech. 3, 457–474. https://doi.org/10.5194/amt-3-457-2010.

Costabile, F., Barnaba, F., Angelini, F., Gobbi, G.P., 2013. Identification of key aerosol populations through their size and composition resolved spectral scattering and absorption. Atmos. Chem. Phys. 13, 2455–2470. https://doi.org/10.5194/acp-13-2455-2013.

Costabile, F., Gilardoni, S., Barnaba, F., Di Ianni, A., Di Liberto, L., Dionisi, D., Manigrasso, M., Paglione, M., Poluzzi, V., Rinaldi, M., Facchini, M.C., Gobbi, G.P., 2017. Characteristics of brown carbon in the urban Po Valley atmosphere. Atmos. Chem. Phys. 17, 313–326. https://doi.org/10.5194/acp-17-313-2017.

De Tomasi, F., Perrone, M.R., 2006. PBL and dust layer seasonal evolution by lidar and radio-sounding measurements over a peninsular site. Atmos. Res. 80, 86–103. https://doi.org/10.1016/j.atmosres.2005.06.010.

Donateo, A., Lo Feudo, T., Marinoni, A., Dinoi, A., Avolio, E., Merico, E., Calidonna, C.R., Contini, D., Bonasoni, P., 2018. Characterization of in situ aerosol optical properties at three observatories in the central Mediterranean. Atmosphere 9, 369. https://doi.org/10.3390/atmos9100369.

Dubovik, O., Holben, B., Eck, T., Smirnov, A., Kaufman, Y., King, M., Tanré, D., Slutsker, I., 2002. Variability of absorption and optical properties of key aerosol types observed in worldwide locations. J. Atmos. Sci. 59, 590–608. https://doi.org/10.1175/1520-0469(2002)059<0590:VOAAOP>2.0.CO;2.

Ealo, M., Alastuey, A., Ripoll, A., Pérez, N., Minguillón, M.C., Querol, X., Pandolfi, M., 2016. Detection of Saharan dust and biomass burning events using near-real-time intensive aerosol optical properties in the north-western Mediterranean. Atmos. Chem. Phys. 16, 12567–12586. https://doi.org/10.5194/acp-16-12567-2016.

Esteve, A.R., Estellés, V., Utrillas, M.P., Martínez-Lozano, J.A., 2012. In-situ integrating nephelometer measurements of the scattering properties of atmospheric aerosols at an urban coastal site in western Mediterranean. Atmos. Environ. 47, 43–50. https://doi.org/10.1016/j.atmosenv.2011.11.043.

Gerasopoulos, E., Andreae, M.O., Zerefos, C., Andreae, T.W., Balis, D., Formenti, P., Merlet, P., Amiridis, V., Papastefanou, C., 2003. Climatological aspects of aerosol optical properties in Northern Greece. Atmos. Chem. Phys. 3, 2025–2041. https://doi.org/10.5194/acp-3-2025-2003.

Giles, D.M., Holben, B.N., Eck, T.F., Sinyuk, A., Smirnov, A., Slutsker, I., Dickerson, R.R., Thompson, A.M., Schafer, J.S., 2012. An analysis of AERONET aerosol absorption properties and classifications representative of aerosol source regions. J. Geophys. Res. 117, D17203. https://doi.org/10.1029/2012JD018127.

Gyawali, M., Arnott, W.P., Zaveri, R.A., Song, C., Moosmüller, H., Liu, L., Mishchenko, M.I., Chen, L.-W.A., Green, M.C., Watson, J.G., Chow, J.C., 2012. Photoacoustic optical properties at UV, VIS, and near IR wavelengths for laboratory generated and winter time ambient urban aerosols. Atmos. Chem. Phys. 12, 2587–2601. https://doi.org/10.5194/acp-12-2587-2012.

Hansen, J., Lacis, A., Rind, D., Russell, G., Stone, P., Fung, I., Lerner, J., 1984. Climate sensitivity: analysis of feedback mechanisms. In: Climate Processes and Climate Sensitivity. American Geophysical Union, pp. 130–163. https://doi.org/10.1029/GM029p0130.

Hansen, J., Sato, M., Ruedy, R., 1997. Radiative forcing and climate response. J. Geophys. Res. 102, 6831–6864. https://doi.org/10.1029/96JD03436.

Haywood, J.M., Ramaswamy, V., 1998. Global sensitivity studies of the direct radiative forcing due to anthropogenic sulfate and black carbon aerosols. J. Geophys. Res. 103, 6043–6058. https://doi.org/10.1029/97JD03426.

Haywood, J.M., Shine, K.P., 1995. The effect of anthropogenic sulfate and soot aerosol on the clear sky planetary radiation budget. Geophys. Res. Lett. 22, 603–606. https://doi.org/10.1029/95GL00075.

IPCC, Climate Change 2013, 2013. The Physical Science Basis, the Working Group I Contribution to the UN IPCC's Fifth Assessment Report (WG1 AR5). Cambridge University Press, New York, USA, pp. 159–254.

Kaufman, Y.J., Smirnov, A., Holben, B.N., Dubovik, O., 2001. Baseline maritime aerosol: methodology to derive the optical thickness and scattering properties. Geophys. Res. Lett. 28, 3251–3254. https://doi.org/10.1029/2001GL013312.

Kaufman, Y.J., Tanré, D., Boucher, O., 2002. A satellite view of aerosols in the climate system. Nature 419, 215–223. https://doi.org/10.1038/nature01091.

Kim, H.S., Chung, Y.C., Lee, S.G., 2012. Analysis of spatial and seasonal distributions of MODIS aerosol optical properties and ground-based measurements of mass concentrations in the Yellow Sea region in 2009. Environ. Monit. Assess. 185, 369–382. https://doi.org/10.1007/s10661-012-2559.

Kinne, S., Schulz, M., Textor, C., Guibert, S., Balkanski, Y., Bauer, S.E., Berntsen, T., Berglen, T.F., Boucher, O., Chin, M., Collins, W., Dentener, F., Diehl, T., Easter, R., Feichter, J., Fillmore, D., Ghan, S., Ginoux, P., Gong, S., Grini, A., Hendricks, J., Herzog, M., Horowitz, L., Isaksen, I., Iversen, T., Kirkevåg, A., Kloster, S., Koch, D., Kristjansson, J.E., Krol, M., Lauer, A., Lamarque, J.F., Lesins, G., Liu, X., Lohmann, U., Montanaro, V., Myhre, G., Penner, J., Pitari, G., Reddy, S., Seland, O., Stier, P.,

Takemura, T., Tie, X., 2006. An AeroCom initial assessment – optical properties in aerosol component modules of global models. Atmos. Chem. Phys. 6, 1815–1834. https://doi.org/10.5194/acp-6-1815-2006.

Kirchstetter, T.W., Novakov, T., Hobbs, P.V., 2004. Evidence that the spectral dependence of light absorption by aerosols is affected by organic carbon. J. Geophys. Res. 109, D21208. https://doi.org/10.1029/2004JD004999.

Lack, D.A., Moosmüller, H., McMeeking, G.R., Chakrabarty, R.K., Baumgardner, D., 2014. Characterizing elemental, equivalent black, and refractory black carbon aerosol particles: a review of techniques, their limitations and uncertainties. Anal. Bioanal. Chem. 406, 99–122. https://doi.org/10.1007/s00216-013-7402-3.

Lee, S., Yoon, S., Kim, S., Kim, Y.P., Ghim, Y.S., Kim, J., Kang, C., Kim, Y.J., Chang, L., Lee, S., 2012. Spectral dependency of light scattering/absorption and hygroscopicity of pollution and dust aerosols in Northeast Asia. Atmos. Environ. 50, 246–254. https://doi.org/10.1016/j.atmosenv.2011.12.026.

Lewis, J.R., Welton, E.J., Molod, A.M., Joseph, E., 2013. Improved boundary layer depth retrievals from MPLNET. J. Geophys. Res. Atmos. 118, 9870–9879. https://doi.org/10.1002/jgrd.50570.

Li, X., Maring, H., Savoie, D., Voss, K., Prospero, J.M., 1996. Dominance of mineral dust in aerosol light-scattering in the North Atlantic trade winds. Nature 380, 416–419. https://doi.org/10.1038/380416a0.

Li, J., Carlson, B.E., Lacis, A.A., 2015. Using single scattering albedo spectral curvature to characterize East Asian aerosol mixtures. J. Geophys. Res. 120, 2037–2052. https://doi.org/10.1002/2014JD022433.

Lohmann, U., Feichter, J., 2005. Global indirect aerosol effects: a review. Atmos. Chem. Phys. 5, 715–737. https://doi.org/10.5194/acp-5-715-2005.

Lowenthal, D., Kumar, N., 2006. Light scattering from sea-salt aerosols at interagency monitoring of protected visual environments (IMPROVE) sites. J. Air Waste Manag. Assoc. 56, 636–642. https://doi.org/10.1080/10473289.2006.10464478.

Lyamani, H., Olmo, F.J., Alados-Arboledas, L., 2008. Light scattering and absorption properties of aerosol particles in the urban environment of Granada, Spain. Atmos. Environ. 42, 2630–2642. https://doi.org/10.1016/j.atmosenv.2007.10.070.

Lyamani, H., Olmo, F.J., Alados-Arboledas, L., 2010. Physical and optical properties of aerosols over an urban location in Spain: seasonal and diurnal variability. Atmos. Chem. Phys. 10, 239–254. https://doi.org/10.5194/acp-10-239-2010.

Mallet, M., Roger, J., Despiau, S., Dubovik, O., Putaud, J., 2003. Microphysical and optical properties of aerosol particles in urban zone during ESCOMPTE. Atmos. Res. 69, 73–97. https://doi.org/10.1016/j.atmosres.2003.07.001.

Mallet, M., Dubovik, O., Nabat, P., Dulac, F., Kahn, R., Sciare, J., Paronis, D., Léon, J.F., 2013. Absorption properties of Mediterranean aerosols obtained from multi-year ground-based remote sensing observations. Atmos. Chem. Phys. 13, 9195–9210. https://doi.org/10.5194/acp-13-9195-2013.

Martinsson, J., Eriksson, A.C., Elbaek Nielsen, I., Berg Malmborg, V., Ahlberg, E., Andersen, C., Lindgren, R., Nyström, R., Nordin, E.Z., Brune, W.H., Svenningsson, B., Swietlicki, E., Boman, C., Pagels, J.H., 2015. Impacts of combustion conditions and photochemical processing on the light absorption of biomass combustion aerosol. Environ. Sci. Technol. 49, 14663–14671. https://doi.org/10.1021/acs.est.5b03205.

Masmoudi, M., Chaabane, M., Tanré, D., Gouloup, P., Blarel, L., Elleuch, F., 2003. Spatial and temporal variability of aerosol: size distribution and optical properties. Atmos. Res. 66, 1–19. https://doi.org/10.1016/S0169-8095(02)00174-6.

Moosmüller, H., Engelbrecht, J.P., Skiba, M., Frey, G., Chakrabarty, R.K., Arnott, W.P., 2012. Single scattering albedo of fine mineral dust aerosols controlled by iron concentration. J. Geophys. Res. 117, D11210. https://doi.org/10.1029/2011JD016909.

Müller, T., 2015. Development of correction factors for aethalometers AE31 and AE33. In: ACTRIS-2 WP3 Workshop, Athens, 10-12 November 2015.

Müller, T., Henzing, J.S., de Leeuw, G., Wiedensohler, A., 2011a. Design and performance of a three-wavelength LED-based total scatter and backscatter integrating nephelometer. Atmos. Meas. Tech. 4, 1291–1303. https://doi.org/10.5194/amt-4-1291-2011.

Müller, T., Schladitz, A., Kandler, K., Wiedensohler, A., 2011b. Spectral particle absorption coefficients, single scattering albedos and imaginary parts of refractive indices from ground based in situ measurements at Cape Verde Island during SAMUM-2. Tellus B 63, 573–588. https://doi.org/10.1111/j.1600-0889.2011.00572.x.

Nousiainen, T., Kandler, K., 2015. Light scattering by atmospheric mineral dust particles. In: Kokhanovsky, A.A. (Ed.), Light Scattering Reviews 9. Springer Praxis Books, Springer, Berlin, Heidelberg, pp. 3–52. https://doi.org/10.1007/978-3-642-37985-7.

Pandolfi, M., Cusack, M., Alastuey, A., Querol, X., 2011. Variability of aerosol optical properties in the western Mediterranean Basin. Atmos. Chem. Phys. 11, 8189–8203. https://doi.org/10.5194/acp-11-8189-2011.

Pandolfi, M., Alados-Arboledas, L., Alastuey, A., Andrade, M., Angelov, C., et al., 2018. A European aerosol phenomenology - 6: scattering properties of atmospheric aerosol particles from 28 ACTRIS sites. Atmos. Chem. Phys. 18, 7877–7911. https://doi.org/10.5194/acp-18-7877-2018.

Perrone, M.R., Burlizzi, P., 2015. Methodologies to obtain aerosol property profiles from three-wavelength elastic lidar signals. Int. J. Rem. Sens. 36, 4748–4773. https://doi.org/10.1080/01431161.2015.1093193.

Perrone, M.R., Romano, S., 2018. Relationship between the planetary boundary layer height and the particle scattering coefficient at the surface. Atmos. Res. 213, 57–69. https://doi.org/10.1016/j.atmosres.2018.04.017.

Perrone, M.R., Tafuro, A.M., Kinne, S., 2012. Dust layer effects on the atmospheric radiative budget and heating rate profiles. Atmos. Environ. 59, 344–354. https://doi.org/10.1016/j.atmosenv.2012.06.012.

Perrone, M., Becagli, S., Garcia Orza, J.A.G., Vecchi, R., Dinoi, A., Udisti, R., Cabello, M., 2013a. The impact of long-range-transport on PM1 and PM2.5 at a Central Mediterranean site. Atmos. Environ. 71, 176–186. https://doi.org/10.1016/j.atmosenv.2013.02.006.

Perrone, M.R., Dinoi, A., Becagli, S., Udisti, R., 2013b. Chemical composition of PM1 and PM2.5 at a suburban site in southern Italy. Int. J. Environ. Anal. Chem. 94, 127–150. https://doi.org/10.1080/03067319 .2013.791978.

Perrone, M.R., Romano, S., Orza, J.A.G., 2014. Particle optical properties at a Central Mediterranean site: impact of advection routes and local meteorology. Atmos. Res. 145–146, 152–167. https://doi.org/10.1016/j.atmosres.2014.03.029.

Perrone, M.R., Romano, S., Orza, J.A.G., 2015. Columnar and ground-level aerosol optical properties: sensitivity to the transboundary pollution, daily and weekly patterns, and relationships. Environ. Sci. Pollut. Res. 22, 16570–16589. https://doi.org/10.1007/s11356-015-4850-7.

Perrone, M.R., Romano, S., Genga, A., Paladini, F., 2018. Integration of optical and chemical parameters to improve the particulate matter characterization. Atmos. Res. 205, 93–106. https://doi.org/10.1016/j.atmosres.2018.02.015.

Petzold, A., Rasp, K., Weinzierl, B., Esselborn, M., Hamburger, T., Dörnbrack, A., Kandler, K., Schütz, L., Knippertz, P., Fiebig, M., Virkkula, A., 2009. Saharan dust absorption and refractive index from aircraft-based observations during SAMUM 2006. Tellus B 61, 118–130. https://doi.org/10.1111/j.1600-0889.2008.00383.x.

Rizza, U., Miglietta, M.M., Mangia, C., Ielpo, P., Morichetti, M., Iachini, C., Virgili, S., Passerini, G., 2018. Sensitivity of WRF-Chem model to land surface schemes: assessment in a severe dust outbreak episode in the Central Mediterranean (Apulia Region). Atmos. Res. 201, 168–180. https://doi.org/10.1016/j.atmosres.2017.10.022.

Rizzo, L.V., Correia, A.L., Artaxo, P., Procópio, A.S., Andreae, M.O., 2011. Spectral dependence of aerosol light absorption over the Amazon Basin. Atmos. Chem. Phys. 11, 8899–8912. https://doi.org/10.5194/acp-11-8899-2011.

Romano, S., Lo Feudo, T., Calidonna, C.R., Burlizzi, P., Perrone, M.R., 2017. Solar eclipse of 20 March 2015 and impacts on irradiance, meteorological parameters, and aerosol properties over southern Italy. Atmos. Res. 198, 11–21. https://doi.org/10.1016/j.atmosres.2017.08.001.

Romano, S., Burlizzi, P., Kinne, S., De Tomasi, F., Hamann, U., Perrone, M.R., 2018. Radiative impact of Etna volcanic aerosols over south eastern Italy on 3 December 2015. Atmos. Environ. 182, 155–170. https://doi.org/10.1016/j.atmosenv.2018.03.038.

Rosenfeld, D., Lensky, I.M., 1998. Satellite-based insights into precipitation formation processes in continental and maritime convective clouds. Bull. Am. Meteorol. Soc. 79, 2457–2476. https://doi.org/10.1175/1520-0477(1998)079<2457:SBIIPF>2.0.CO;2.

Russell, P.B., Bergstrom, R.W., Shinozuka, Y., Clarke, A.D., De Carlo, P.F., Jimenez, J.L., Livingston, J.M., Redemann, J., Dubovik, O., Strawa, A., 2010. Absorption Ångström Exponent in AERONET and related data as an indicator of aerosol composition. Atmos. Chem. Phys. 10, 1155–1169. https://doi.org/10.5194/acp-10-1155-2010.

Russell, P.B., Kacenelenbogen, M., Livingston, J.M., Hasekamp, O.P., Burton, S.P., Schuster, G.L., Johnson, M.S., Knobelspiesse, K.D., Redemann, J., Ramachandran, S., Holben, B., 2014. A Multi-parameter aerosol classification method and its application to retrievals from spaceborne polarimetry. J. Geophys. Res. Atmos. 119, 9838–9863. https://doi.org/10.1002/2013JD021411.

Saha, A., Mallet, M., Roger, J., Dubuisson, P., Piazzola, J., Despiau, S., 2008. One year measurements of aerosol optical properties over an urban coastal site: effect on local direct radiative forcing. Atmos. Res. 90, 195–202. https://doi.org/10.1016/j.atmosres.2008.02.003.

Santese, M., De Tomasi, F., Perrone, M.R., 2008. Advection patterns and aerosol optical and microphysical properties by AERONET over south-east Italy in the central Mediterranean. Atmos. Chem. Phys. 8, 1881–1896. https://doi.org/10.5194/acp-8-1881-2008.

Saturno, J., Pöhlker, C., Massabò, D., Brito, J., Carbone, S., Cheng, Y., Chi, X., Ditas, F., Hrabě de Angelis, I., Morán-Zuloaga, D., Pöhlker, M.L., Rizzo, L.V., Walter, D., Wang, Q., Artaxo, P., Prati, P., Andreae, M.O., 2017. Comparison of different Aethalometer correction schemes and a reference multi-wavelength absorption technique for ambient aerosol data. Atmos. Meas. Tech. 10, 2837–2850. https://doi.org/10.5194/amt-10-2837-2017.

Schmeisser, L., Andrews, E., Ogren, J.A., Sheridan, P., Jefferson, A., Sharma, S., Kim, J.E., Sherman, J.P., Sorribas, M., Kalapov, I., Arsov, T., Angelov, C., Mayol-Bracero, O.L., Labuschagne, C., Kim, S.-W., Hoffer, A., Lin, N.-H., Chia, H.-P., Bergin, M., Sun, J., Liu, P., Wu, H., 2017. Classifying aerosol type using in situ surface spectral aerosol optical properties. Atmos. Chem. Phys. 17, 12097–12120. https://doi.org/10.5194/acp-17-12097-2017.

Schmid, O., Artaxo, P., Arnott, W.P., Chand, D., Gatti, L.V., Frank, G.P., Hoffer, A., Schnaiter, M., Andreae, M.O., 2006. Spectral light absorption by ambient aerosols influenced by biomass burning in the Amazon Basin. I: comparison and field calibration of absorption measurement techniques. Atmos. Chem. Phys. 6, 3443–3462. https://doi.org/10.5194/acp-6-3443-2006.

Schuster, G.L., Dubovik, O., Holben, B.N., 2006. Ångström exponent and bimodal aerosol size distributions. J. Geophys. Res. 111, D07207. https://doi.org/10.1029/2005JD006328.

Seidel, D.J., Zhang, Y., Beljaars, A., Golaz, J.C., Jacobson, A.R., Medeiros, B., 2012. Climatology of the planetary boundary layer over the continental United States and Europe. J. Geophys. Res. 117, D17106. https://doi.org/10.1029/2012JD018143.

Seinfeld, J.H., Pandis, S.N., 1998. Atmospheric Chemistry and Physics: from Air Pollution to Climate Change. J. Wiley &Sons, INC.

Ten Brink, H.M., Veefkind, J.P., Waijers-IJpelaan, A., van der Hage, J.C.H., 1996. Aerosol light-scattering in The Netherlands. Atmos. Environ. 30, 4251–4261. https://doi.org/10.1016/1352-2310(96) 00091-X.

Titos, G., Foyo-Moreno, I., Lyamani, H., Querol, X., Alastuey, A., Alados-Arboledas, L., 2012. Optical properties and chemical composition of aerosol particles at an urban location: an estimation of the aerosol mass scattering and absorption efficiencies. J. Geophys. Res. 117, D04206. https://doi.org/10.1029/2011JD016671.

Titos, G., Cazorla, A., Zieger, P., Andrews, E., Lyamani, H., Granados-Muñoz, M.J., Olmo,

F.J., Alados-Arboledas, L., 2016. Effect of hygroscopic growth on the aerosol light scattering coefficient: a review of measurements, techniques and error sources. Atmos. Environ. 141, 494–507. https://doi.org/10.1016/j.atmosenv.2016.07.021.

Titos, G., del Águila, A., Cazorla, A., Lyamani, H., Casquero-Vera, J.A., Colombi, C., Cuccia, E., Gianelle, V., Mo, G., Alastuey, A., Olmo, F.J., Alados-Arboledas, L., 2017. Spatial and temporal variability of carbonaceous aerosols: assessing the impact of biomass burning in the urban environment. Sci. Total Environ. 578, 613–625. https://doi.org/10.1016/j.scitotenv.2016.11.007.

Toledano, C., Cachorro, V., Berjon, A., De Frutos, A., Sorribas, M., De la Morena, B., Goloub, P., 2007. Aerosol optical depth and Ångström exponent climatology at El Arenosillo AERONET site (Huelva, Spain). Q. J. R. Meteorol. Soc. 133 (624), 795–807. https://doi.org/10.1002/qj.54.

Weingartner, E., Saathoff, H., Schnaiter, M., Streit, N., Bitnar, B., Baltensperger, U., 2003. Absorption of light by soot particles: determination of the absorption coefficient by means of aethalometers. J. Aerosol Sci. 34, 1445–1463. https://doi.org/10.1016/S0021-8502(03)00359-8.

Yang, M., Howell, S.G., Zhuang, J., Huebert, B.J., 2009. Attribution of aerosol light absorption to black carbon, brown carbon, and dust in China – interpretations of atmospheric measurements during EAST-AIRE. Atmos. Chem. Phys. 9, 2035–2050. https://doi.org/10.5194/acp-9-2035-2009.

Yu, H., Kaufman, Y.J., Chin, M., Feingold, G., Remer, L.A., Anderson, T.L., Balkanski, Y., Bellouin, N., Boucher, O., Christopher, S., DeCola, P., Kahn, R., Koch, D., Loeb, N., Reddy, M.S., Schulz, M., Takemura, T., Zhou, M., 2006. A review of measurement-based assessments of the aerosol direct radiative effect and forcing. Atmos. Chem. Phys. 6, 613–666. https://doi.org/10.5194/acp-6-613-2006.

Yu, H., Remer, L., Kahn, R., Chin, M., Zhang, Y., 2013. Satellite perspective of aerosol intercontinental transport: from qualitative tracking to quantitative characterization. Atmos. Res. 124, 73–100. https://doi.org/10.1016/j.atmosres.2012.12.013.

Zhang, X.Y., Wang, Y.Q., Niu, T., Zhang, X.C., Gong, S.L., Zhang, Y.M., Sun, J.Y., 2012. Atmospheric aerosol compositions in China: spatial/temporal variability, chemical signature, regional haze distribution and comparisons with global aerosols. Atmos. Chem. Phys. 12, 779–799. https://doi.org/10.5194/acp-12-779-2012.

Zieger, P., Fierz-Schmidhauser, R., Poulain, L., Müller, T., Birmili, W., Spindler, G., Wiedensohler, A., Baltensperger, U., Weingartner, E., 2014. Influence of water uptake on the aerosol particle light scattering coefficients of the Central European aerosol. Tellus B 66, 22716. https://doi.org/10.3402/tellusb.v66.22716.

Zieger, P., Väisänen, O., Corbin, J.C., Partridge, D.G., Bastelberger, S., Mousavi-Fard, M., Rosati, B., Gysel, M., Krieger, U.K., Leck, C., Nenes, A., Riipinen, I., Virtanen, A., Salter, M.E., 2017. Revising the hygroscopicity of inorganic sea salt particles. Nat. Commun. 8, 15883. https://doi.org/10.1038/ncomms15883.

Zotter, P., Herich, H., Gysel, M., El-Haddad, I., Zhang, Y., Močnik, G., Hüglin, C., Baltensperger, U., Szidat, S., Prévôt, A.S.H., 2017. Evaluation of the absorption Ångström exponents for traffic and wood burning in the Aethalometer-based source apportionment using radiocarbon measurements of ambient aerosol. Atmos. Chem. Phys. 17, 4229–4249. https://doi.org/10.5194/acp-17-4229-2017.